Analysis of daily, monthly, and annual burned area using the fourth-generation global fire emissions database (GFED4)

Louis Giglio,[1] James T. Randerson,[2] and Guido R. van der Werf[3]

[1]   We describe the fourth generation of the Global Fire Emissions Database (GFED4) burned area data set, which provides global monthly burned area at 0.25° spatial resolution from mid-1995 through the present and daily burned area for the time series extending back to August 2000. We produced the full data set by combining 500 m MODIS burned area maps with active fire data from the Tropical Rainfall Measuring Mission (TRMM) Visible and Infrared Scanner (VIRS) and the Along-Track Scanning Radiometer (ATSR) family of sensors. We found that the global annual area burned for the years 1997 through 2011 varied from 301 to 377 Mha, with an average of 348 Mha. We assessed the interannual variability and trends in burned area on the basis of a region-specific definition of fire years. With respect to trends, we found a gradual decrease of 1.7 Mha yr^{-1} (–1.4% yr^{-1}) in Northern Hemisphere Africa since 2000, a gradual increase of 2.3 Mha yr^{-1} (+1.8% yr^{-1}) in Southern Hemisphere Africa also since 2000, a slight increase of 0.2 Mha yr^{-1} (+2.5% yr^{-1}) in Southeast Asia since 1997, and a rapid decrease of approximately 5.5 Mha yr^{-1} (–10.7% yr^{-1}) from 2001 through 2011 in Australia, followed by a major upsurge in 2011 that exceeded the annual area burned in at least the previous 14 years. The net trend in global burned area from 2000 to 2012 was a modest decrease of 4.3 Mha yr^{-1} (–1.2% yr^{-1}). We also performed a spectral analysis of the daily burned area time series and found no vestiges of the 16 day MODIS repeat cycle.

1. Introduction

[2]   The Global Fire Emissions Database (GFED) [*van der Werf et al.*, 2006, 2010] is one of a growing number of large-scale fire emissions inventories developed to help elucidate the role of biomass burning in the global carbon cycle and within the Earth system as a whole. Other inventories include the *Urbanski et al.* [2011] Wildland Fire Emission Inventory (WFEI), the *Hoelzemann et al.* [D14S04] Global Wildland Fire Emission Model (GWEM), the *Lamarque et al.* [2010] Emissions for Atmospheric Chemistry and Climate Model Intercomparison Project (ACCMIP) inventory, the *Liousse* [2010] African Monsoon Multidisciplinary Analysis (AMMA) biomass burning inventory, and the *Schultz et al.* [2008] RETRO wildfire emissions data set. Almost without exception, each inventory includes an underlying burned area component used to formulate emissions, from which independent insight can be obtained about ecosystem and Earth system processes. For the third and most recent version of GFED ("GFED3"), this component had a monthly time step and a spatial resolution of 0.5°.

[3]   Here we describe the fourth generation of the GFED burned area data set—GFED4—which provides global monthly burned area at 0.25° spatial resolution from mid-1995 through the present and daily burned area for a subset of the time series extending back to August 2000. As with previous versions of GFED, the data set is primarily intended for use within large-scale atmospheric and biogeochemical models and for interpreting regional and continental-scale controls on fire activity from climate and different forms of land management. We provide a summary of the remotely sensed input data sets used in this work in section 2, followed by a description of our methods in section 3. In section 4, we perform some basic analyses using the monthly GFED4 data set, including a comparison with GFED3. Next, in section 5, we assess the long-term trends and interannual variability in global and regional burned area over the past 16 years. In section 6, we examine the GFED4 daily time series and describe the results of a simple spectral analysis, and in section 7, we discuss several

---

Additional supporting information may be found in the online version of this article.

[1]Department of Geogaphical Sciences, University of Maryland, College Park, Maryland, USA.

[2]Department of Earth System Science, University of California, Irvine, California, USA.

[3]Faculty of Earth and Life Sciences, VU University, Amsterdam, The Netherlands.

Corresponding author: L. Giglio, Department of Geographical Sciences, University of Maryland, 2181 Lefrak Hall, College Park, MD 20742 , USA. (lgiglio@umd.edu)

caveats and limitations of the data set. Finally, in section 8, we summarize our findings and consider the prospect of extending GFED into the future as well as further into the past.

2. Data

2.1. Burned Area Data

[4] We used the 500 m Collection 5.1 MODIS direct broadcast (DB) burned area product (MCD64A1), now produced globally using the *Giglio et al.* [2009] MODIS DB burned-area mapping algorithm. The algorithm identifies the date of burn (to the nearest day) for each grid cell within individual MODIS Level 3 tiles [*Wolfe et al.*, 1998]. The Collection 5.1 product incorporates two improvements over the Collection 5 product used in the preparation of GFED3: (1) the final spatial cleaning phase of the original algorithm was relaxed in croplands to reduce the unintentional removal of small agricultural burns, and (2) the product was generated using an alternate "upstream" MODIS daily surface reflectance input product to eliminate systematic omission errors in several MODIS tiles located within the tropics (in these tiles, the Collection 5 surface reflectance data were often inadvertently purged of burned pixels due to an aggressive aerosol-contamination filtering scheme). At present, validation of the MCD64A1 product is limited to Southern Africa, Siberia, Central Asia, Alaska, and the western conterminous United States through comparison with high-resolution Landsat imagery [*Giglio et al.*, 2009; *Loboda et al.*, 2011, 2012; *Tsela et al.*, 2010]. We aggregated the monthly MCD64A1 product to generate global gridded daily and monthly burned area maps at 0.25° spatial resolution. In addition to providing straightforward backward compatibility with GFED3, the choice of a 0.25° bin size and monthly time step was dictated by limitations of the fire data available prior to the advent of MODIS.

2.2. Active Fire Data

[5] We used the algorithm 2 Along-Track Scanning Radiometer (ATSR) World Fire Atlas [*Arino and Rosaz*, 1999], available from June through July 1995 and July 1996 through September 2011, to generate monthly gridded 0.25° ATSR fire counts, and the *Giglio et al.* [2003a] monthly 0.5° Visible and Infrared Scanner (VIRS) fire product from January 1998 through June 2011. To attain the common 0.25° spatial resolution needed in this work, we used coverage information available in the 0.5° VIRS product in conjunction with daily VIRS fire pixel locations to produce a higher resolution, 0.25° monthly VIRS fire data set that included a simple correction for the variable number of satellite overpasses available in each grid cell (cf. Figure 4 of *Giglio et al.* [2003b]).

3. Method

[6] As with the succession of GFED2 by GFED3, the increased (and now complete) coverage of 500 m MODIS burned area maps have allowed us to incorporate significant refinements into GFED4. Foremost among these was an increase in the spatial resolution of the global grid, in this case from 0.5° to 0.25°. In addition, the traditional GFED monthly temporal resolution has been supplemented with
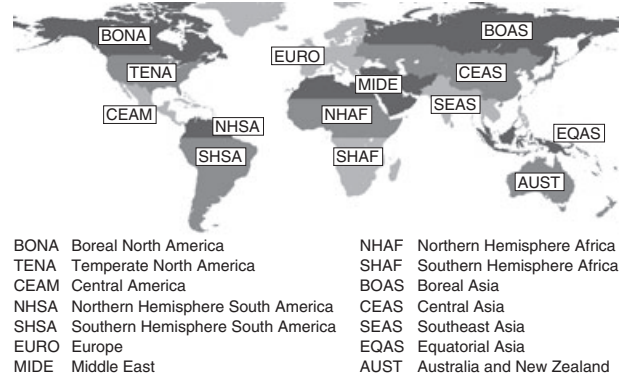

Figure 1. Map of the 14 GFED regions used in this study, after *Giglio et al.* [2010].

a daily version of the product for that portion of the time series spanning the "MODIS era" (August 2000 to present), when high quality MODIS surface reflectance data needed to generate the MCD64A1 product are available.

3.1. Monthly Burned Area

[7] For the MODIS era, the GFED4 monthly burned area data set was derived exclusively from the 500 m MCD64A1 burned area product aggregated to 0.25° spatial resolution on a monthly basis. As with previous versions of GFED, we extended the monthly GFED4 time series into the pre-MODIS era by calibrating monthly active fire counts from the VIRS and ATSR sensors to monthly burned area supplied by the MCD64A1 product. We used a modified version of the model employed by *Giglio et al.* [2010] to express the monthly area burned A in the 0.25° grid cell at location i during month t as a nonlinear function of monthly fire counts $N_f(i,t)$:

$$A(i,t) = \begin{cases} \alpha(i)N_f(i,t)^{\beta(i)} & \text{for } N_f(i,t) > 0 \quad (1a) \\ \phi_r(t)A_c(i,t_c) & \text{for } N_f(i,t) = 0. \quad (1b) \end{cases}$$

Here $\alpha(i) \geq 0$ and $\beta(i) > 0$ are regression parameters fitted independently for each grid cell, $A_c(i,t_c)$ is the climatological monthly burned area for the grid cell during the calendar month t_c of time step t, and $\phi_r(t)$ is a *monthly climatology adjustment factor* for the region r in which the grid cell resides (Figure 1). The monthly climatology was derived from the August 2000 through December 2011 aggregated MCD64A1 burned area product. The regional climatology adjustment factor $\phi_r(t)$ for a given month is defined as the capped ratio of the total number of fire pixels detected in region r during month t to the monthly fire-pixel climatology for the region. Specifically,

$$\phi_r(t) = \min\left(\frac{\sum_{i \in r} N_f(i,t)}{\sum_{i \in r} \sum_{\tau \in t_c} N_f(i,\tau)}, \phi_{\max,r}\right), \quad (2)$$

where the function $\min(a,b)$ yields the lesser of a and b. The constant $\phi_{\max,r}$ constrains the adjustment factor such that $\phi_r(t) \leq \phi_{\max,r}$ and was computed independently for each region using an optimization procedure that minimized the mean absolute error between the burned area predicted via equation (1b) annually from 2003 to 2010 and the corresponding annual MCD64A1 "ground truth" totals

(see Table S1 and Figure S1 of Text S1 of the supporting information). The adjustment factors were computed separately for the VIRS and ATSR sensors.

3.1.1. Use of Burned Area Climatology

[8] The use of a climatology in equation (1) is a departure from earlier approaches used in GFED with the following rationale. As has been noted previously [*Giglio et al.*, 2006, 2010], the comparatively sparse temporal sampling of the VIRS and ATSR sensors leads to large numbers of grid cells in which active fires are never detected yet which contain burned area. The cumulative effect of these empty grid cells over large spatial and temporal scales is to underestimate the total area burned [*Giglio et al.*, 2010]. For GFED3, we employed region-specific correction factors that boosted the burned area estimates to compensate for this loss, an approach that was not entirely satisfactory as it did nothing to fill in the spatial gaps in burned area caused by the empty grid cells in the first place. For the ATSR, these gaps can span many hundreds of kilometers in Africa due to the particularly strong diurnal fire cycle characteristic of this region [*Giglio*, 2007]. For GFED4, we deemed the "painting in" of burned area into grid cells persistently devoid of fire pixels but replete with burned area as more realistic than the regional scaling applied in GFED3.

[9] Our motivation for constraining the regional adjustment factors $\phi_r(t)$ lies in recognition of the fact that the larger number of ATSR and VIRS fire pixels detected during years of high fire activity are most often associated with relatively large individual fires that have a much higher likelihood of being detected from space. The resulting surplus of fire pixels will be reflected in the proximate values of $N_f(i, t)$, thus boosting the estimate of burned area predicted with equation (1a). It is consequently prudent to limit the impact these surplus fire pixels have on $\phi_r(t)$, as not doing so could essentially "double count" their contribution to the total burned area estimated for each region. In effect, we are maintaining that a negative anomaly in monthly fire counts for a particular region is more likely to represent a general decrease in fire activity throughout the region, whereas a positive fire-count anomaly is more likely to represent localized patches of increased fire activity that are in turn more likely to be captured in the monthly fire counts of the proximate grid cells.

3.1.2. Uncertainties

[10] For GFED4, estimation of one-standard-deviation uncertainties in monthly burned area $\sigma_A(i, t)$ followed the methodology used by *Giglio et al.* [2010]. In that approach, the total uncertainty σ_A is a combination of the inherent uncertainty σ_B in binning potentially misclassified 500 m pixels from the MCD64A1 product into a 0.25° grid cell and the regression uncertainty σ_R when using equation (1a) to estimate burned area during the pre-MODIS era. Details may be found in *Giglio et al.* [2010].

3.2. Daily Burned Area

[11] The GFED4 daily burned area data set was derived exclusively from the 500 m MCD64A1 burned area product aggregated to 0.25° spatial resolution on a daily basis. No attempt was made to extend the daily data set into the pre-MODIS era because at this spatial resolution neither VIRS nor ATSR fire counts provide any practical capability to predict burned area at time scales much shorter than 1 month

[*Giglio et al.*, 2010]. Further complicating any attempt to use VIRS fire observations on a near-daily basis is the presence of major sampling artifacts in the daily time series as the TRMM overpass drifts through the diurnal fire cycle prevalent in most regions [*Giglio et al.*, 2003b; *Giglio*, 2007].

3.2.1. Uncertainties in Burn Date

[12] The underlying MCD64A1 burned area maps include an estimate of the uncertainty in the burn date associated with each burned 500 m pixel. This uncertainty typically varies from ±1 day under clear sky conditions to ±5 days during intervals in which clouds obscure up to about 75% of daily scenes. Under more persistent cloud cover, e.g., as low as 15% of scenes cloud-free, the uncertainty is much larger (±20 days and higher), and with still higher cloud cover no mapping is possible at all. A feature exploited in assigning uncertainties to each 0.25° GFED monthly burned area estimate is that the MCD64A1 temporal uncertainty is usually much smaller than the ∼30 day aggregation period of the monthly product. Clearly such an assumption does not apply to the daily GFED4 time series. For this reason, the temporal uncertainties of individual 500 m burned pixels are averaged for each 0.25° grid cell to produce spatially explicit temporal uncertainty estimates (the "mean burn-date uncertainty") in the daily product.

3.2.2. August 2000 and June 2001 Data Outages

[13] The Terra MODIS instrument experienced two extended outages from 6 to 18 August 2000 and 16 June to 2 July 2001. The ensuing data gaps degrade the accuracy of the MCD64A1 burned area maps spanning those time periods in two specific ways. First, the likelihood of both omission and commission errors will increase due to the potential removal of abrupt changes associated with burning from the time series and the potential introduction of an artificial abrupt change in the time series. Second, the uncertainty in burn date will grow at least as large as the duration of the outage. For burns that appear to occur during periods of missing data, the MCD64A1 mapping algorithm conservatively estimates the burn date in the middle of the gap. While not unreasonable at the scale of a single MODIS tile, this methodology has the side effect of introducing enormous spikes on two specific days (12 August 2000 and 24 June 2001) of the global daily burned area time series. To remove these unrealistic artifacts from the global data set, we uniformly redistributed the total burned area detected in each grid cell during each outage period on a daily basis.

3.3. Merging of Burned Area Estimates

[14] For consistency, merging of the different burned area sources was performed during the pre-MODIS era in essentially the same manner as for GFED3, with minor differences reflecting the use of the burned area climatology in GFED4. ATSR fire counts were used to estimate burned area in the high-latitude regions [Boreal North America (BONA) and Boreal Asia (BOAS)] as well as Southern Hemisphere Africa (SHAF), Central Asia (CEAS), and Equatorial Asia (EQAS), while VIRS fire counts were used in Northern Hemisphere South America (NHSA), Southern Hemisphere South America (SHSA), Northern Hemisphere Africa (NHAF), and Australia and New Zealand (AUST). Burned area estimates from the two sensors were merged in the remaining regions, with VIRS estimates having

precedence when available. Prior to January 1998, the GFED4 burned area time series was produced exclusively from ATSR observations and the MDC64A1 burned area climatology.

3.4. Ancillary Data Layers

[15] The daily and monthly GFED4 burned area data sets incorporate updates to the ancillary data layers introduced in GFED3. These include the following: (1) the distribution of burned area within each grid cell as a function of fractional tree cover, based on the *Townshend et al.* [2011] 250 m MODIS Collection-5 Vegetation Continuous Fields product (MOD44B); (2) a breakdown of burned area within the grid cell by land cover type, based on the
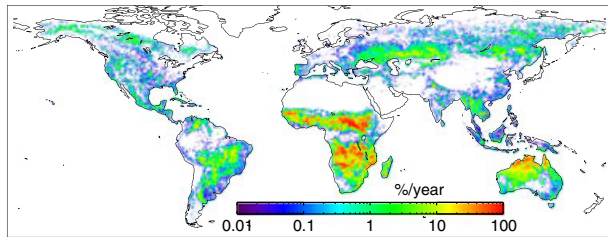

Figure 2. Mean annual area burned, expressed as the fraction of each grid cell that burns each year, derived from the July 1996 to August 2012 monthly GFED4 burned area time series.

Friedl et al. [2010] 500 m MODIS Collection-5 land cover product (MCD12Q1); and (3) the fraction of burned area observed in organic peat in Indonesia. For the MODIS era, we compiled these fields using the locations of individual 500 m MCD64A1 burned area pixels within each 0.25° grid cell; for the pre-MODIS era, we compiled the fields based on the locations of individual VIRS or ATSR active fire pixels within each grid cell. As with GFED3, an additional monthly fire persistence data layer is provided in the monthly burned area data set for its utility in identifying deforestation fires [*Giglio et al.*, 2006].

4. Analysis Using Monthly Time Series

4.1. Spatial Distribution and Monthly Time Series

[16] In Figure 2, we show the spatial distribution of burned area for the July 1996 to August 2012 time period, expressed as the average fraction of a grid cell that burns each calendar year (see also Figures S2–S7 of Text S1). Particularly notable at this scale is the large contiguous patch in southern Chad, the Central African Republic, and South Sudan, which to first order burns in its entirety each year (Figure S4 of Text S1). Fires in this sparsely populated open savanna (comprising much of the East Sudanian savanna ecoregion) are driven by the hot Harmattan trade winds virtually unchecked during the dry season [*Pereira et al.*, 2000].

[17] The monthly burned area time series for each region is shown in Figure 3. Because ATSR fire data were
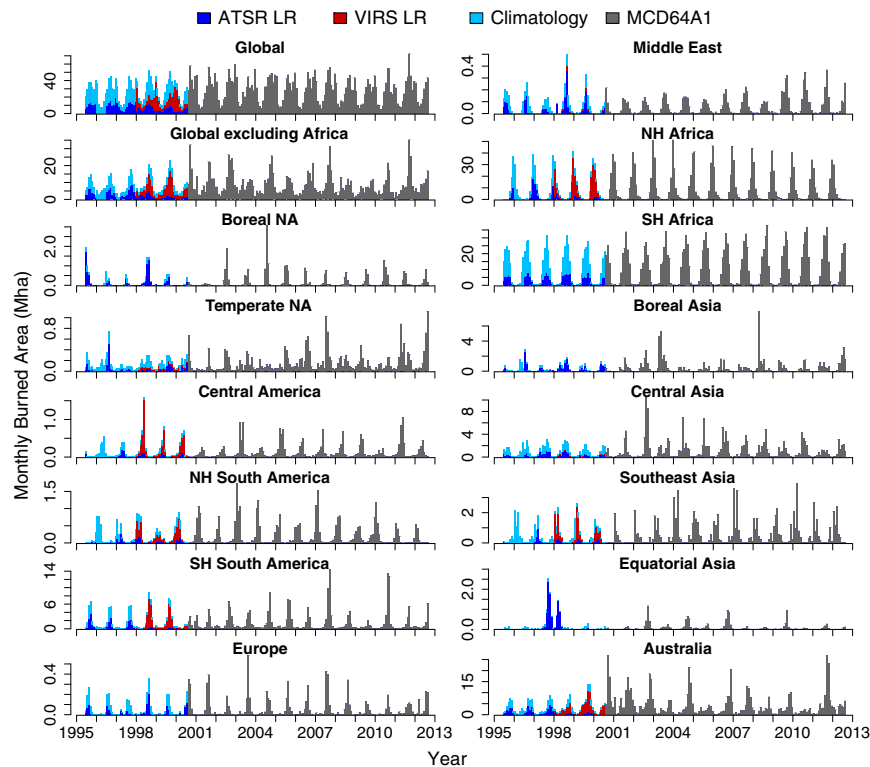

Figure 3. Regional and worldwide July 1995 to August 2012 time series of GFED4 monthly burned area. The different colors indicate the contribution from each of the different data sources and methodologies (ATSR and VIRS local regression [LR], climatology, 500 m MCD64A1 burned area maps) used to produce the entire data set.
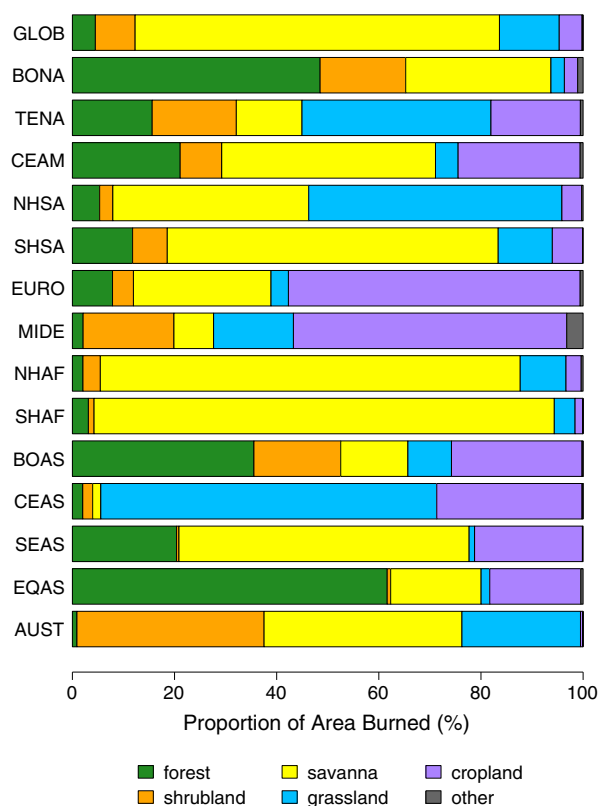
Figure 4. Proportion of burned area within specific land cover types from July 1996 to August 2012 for the entire globe (GLOB) and the regions shown in Figure 1.

Figure 5. Change between GFED3 and GFED4 mean annual burned area, relative to GFED3, computed using common subsets of the respective products from the pre-MODIS era (July 1996 to July 2000, dark gray bars), and the MODIS era (August 2000 to February 2012, light gray bars). Positive values indicate an increase in burned area in GFED4 compared to GFED3, while negative values indicate a decrease.

unavailable from January to June 1996, GFED4 relies solely on the burned area climatology for this period.

4.2. Land Cover Distribution

[18] The distribution of area burned by land cover type is shown for each region in Figure 4, again for the July 1996 to August 2012 time period. To simplify the analysis, we aggregated the 15 distinct University of Maryland land cover classes present in the MCD12Q1 land cover product into six broader classes (*forest*, *shrubland*, *savanna*, *grassland*, *cropland*, and *other*). In terms of area burned, savanna fires were overwhelmingly dominant in both Southern Hemisphere (SH) and Northern Hemisphere (NH) Africa (90% and 82% of the total area burned, respectively), and somewhat less so in SH South America (65%). With the bulk of the area burned worldwide each year residing in Africa, savanna fires comprise the largest proportion (71%) of area burned at the global scale as well. Forest fires (either wildfires or those burning in the deforestation process) comprised the largest proportion of area burned in Equatorial Asia (62%), followed by Boreal North America (48%) and Boreal Asia (36%). Grassland fires were the most prevalent in Central Asia and NH South America, while cropland fires were dominant in Europe and the Middle East. Shrubland burning comprised a relatively small proportion of the area burned in all regions except Australia, where 37% of the area burned belonged to this category.
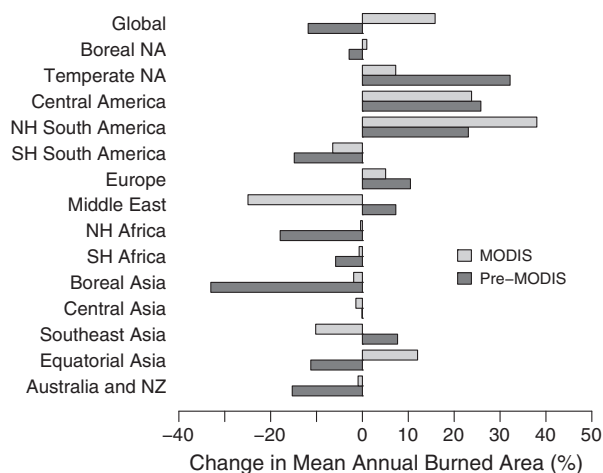
4.3. Comparison with GFED3

[19] We compared our GFED4 burned area data set to GFED3 for both the MODIS and pre-MODIS eras. The regional differences are shown in Figure 5, which depicts the relative change in burned area from GFED3 to GFED4. As with the transition from GFED2 to GFED3, the magnitude of the change varied considerably by region. In most cases, a change in burned area during the MODIS era was accompanied by a change in burned area during the pre-MODIS era in the same direction (i.e., with the same sign). This is expected since the MODIS-era burned area maps were used to calibrate the pre-MODIS active fire data. Nontrivial exceptions to this behavior are noted in the Middle East (MIDE), Southeast Asia (SEAS), and EQAS. These counterintuitive cases arise primarily as a consequence of the use of 45 additional months of ATSR fire data for calibration and the higher spatial resolution of GFED4. In using this larger set of observations to fit the nonlinear model in equation (1a), the new regression-based burned area estimates may well decrease. EQAS has the further complication of exhibiting extremely high and unprecedented ATSR and VIRS active fire counts in some grid cells during the 1997–1998 El-Niño Southern Oscillation (ENSO) that were wholly absent from the training data used for calibration. The unavoidable extrapolation in this situation can produce considerably different burned area estimates when the same model is calibrated over different spatial scales.

[20] The differences between GFED3 and GFED4 during the MODIS era arise for two reasons. First, additional MCD64A1 maps were incorporated into GFED4, providing 100% coverage of the land surface at 500 m spatial resolution from August 2000 onward (for GFED3 the MODIS burned area maps still had significant gaps in global coverage). Second, GFED3 and GFED4 were produced

using two different versions of the MCD64A1 burned area product, and clearly those changes made for Collection 5.1 (see section 2.1) will be reflected in GFED4.

5. Trends and Interannual Variability

[21] Following the recommendation of *Boschetti and Roy* [2008], we analyzed the regional interannual variability of

burned area with respect to a fire year appropriate for each region. A fire year brackets a complete burning season and in general does not coincide with a calendar year (which may interrupt a fire season while it remains fully active, as in the case of NH Africa burning most heavily in December and January). The notion of a fire year becomes somewhat ambiguous in regions or at scales having no distinct period of fire activity (or, equivalently, no distinct period without
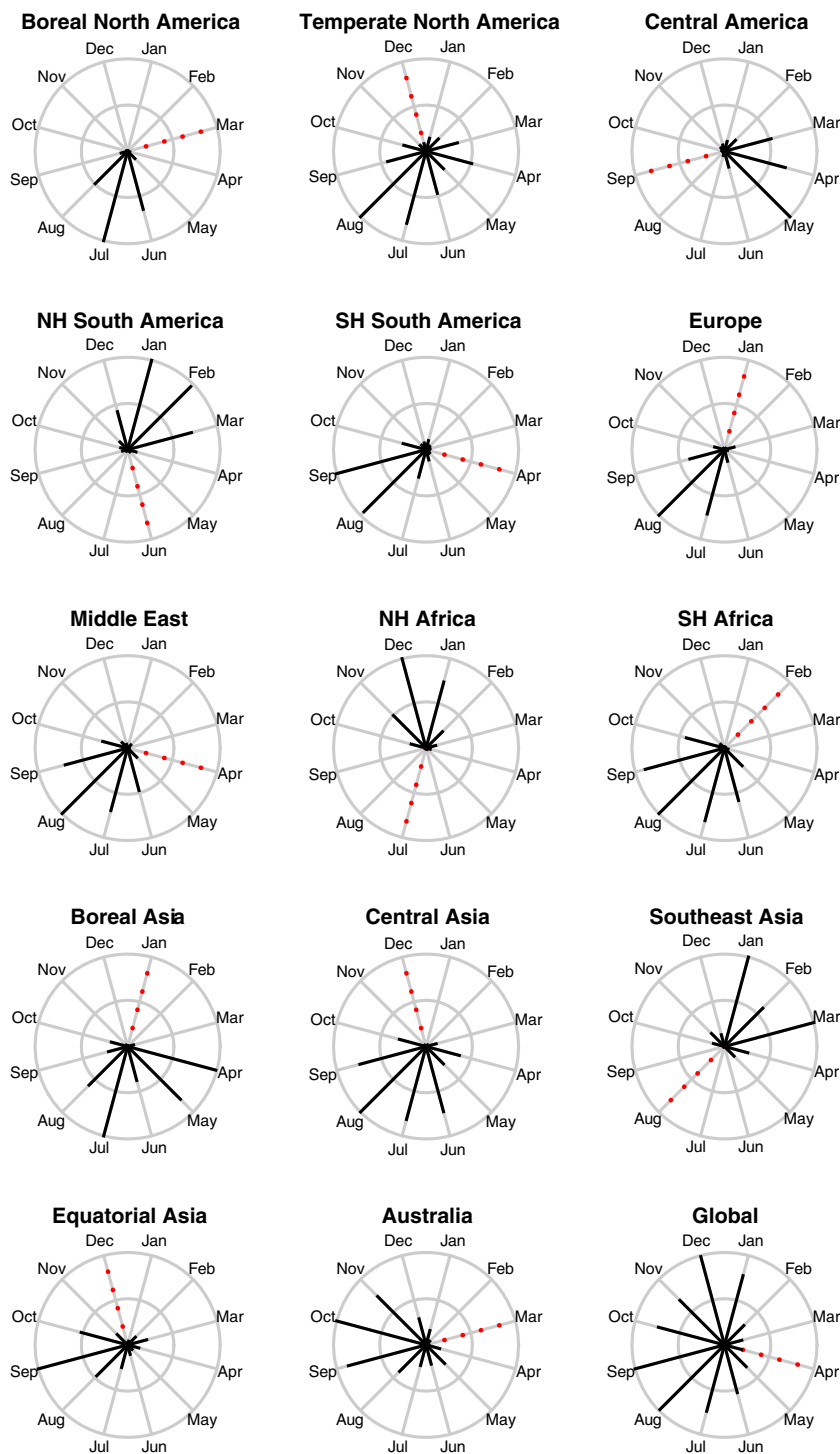

Figure 6. Normalized monthly GFED4 burned area climatologies derived from the monthly data set for the July 1996 to August 2012 time period. For each region, the dotted red line indicates the calendar month of minimum burned area.

fire activity), but aside from the global case such regions are relatively rare.

[22] We defined a fire year for each region using a ~15 year monthly burned area climatology generated from our GFED4 data set (Figure 6). Here we deviated from *Boschetti and Roy* [2008], who advocated using specific metrics based on temporal derivatives to define an optimal fire year, by adopting the following simple convention: The last calendar month of the 12 month fire year for a given region is that calendar month for which the monthly climatological burned area was a minimum. (For a justification of this convention, see section S3 of Text S1.) Based on this criterion, we computed successive 12 month burned area totals for each region from ~July 1996 onward (the exact start month varied by region), which we then analyzed with respect to trends and interannual variability.

5.1. Trends

[23] In Figure 7, we show the annual area burned within each GFED region, summarized in terms of region-specific fire years as discussed above. (See Tables S2 and S3 in Text S1 for a traditional summary of annual area burned
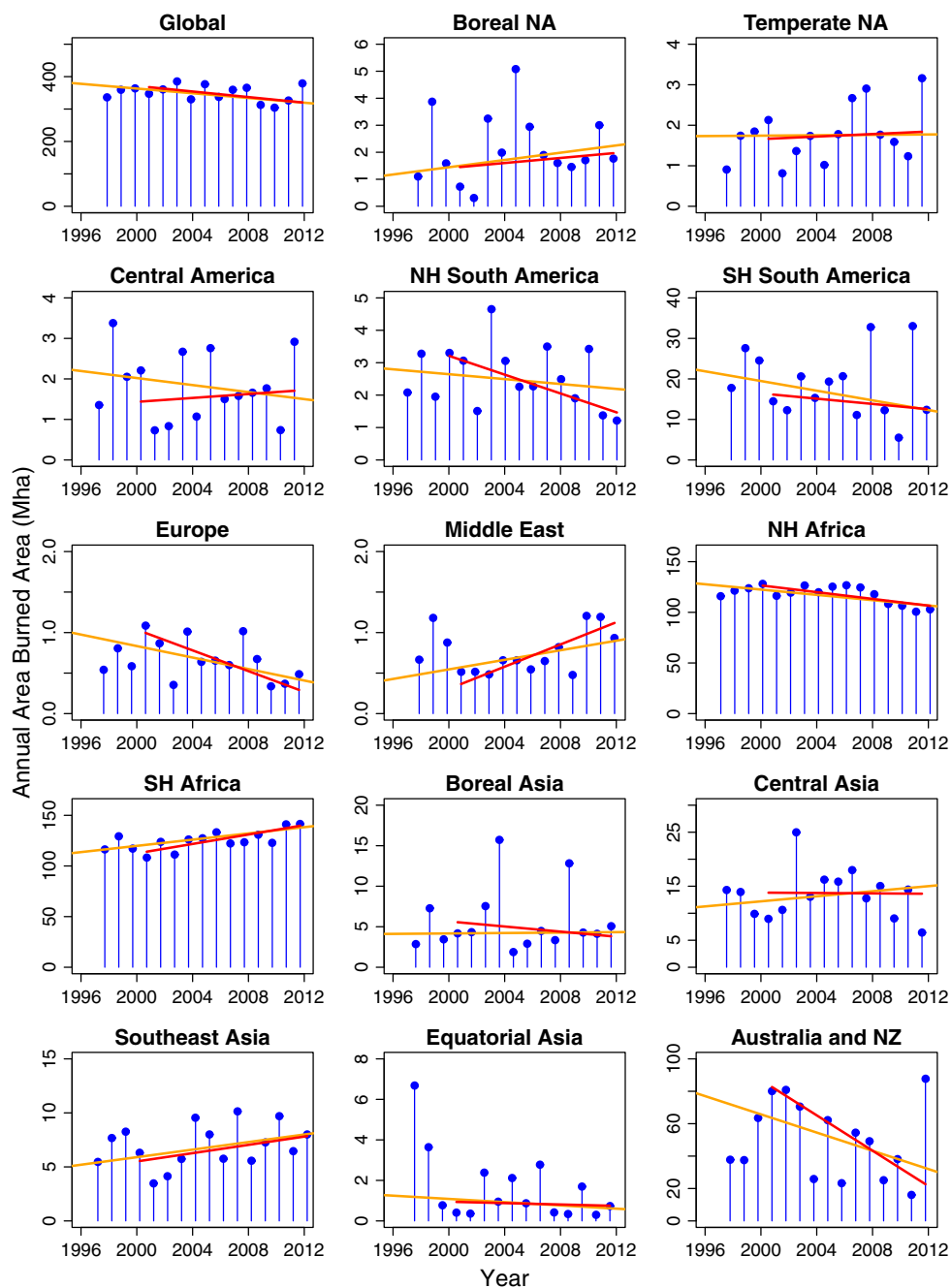

Figure 7. Annual worldwide and regional GFED4 burned area time series spanning 1996 through mid-2012, summarized on the basis of region-specific fire years as defined in Figure 6. Trend lines were fitted to the full GFED4 time series (orange lines) as well as the MODIS-era subset (red lines).

Table 1. Absolute and Relative Trends in Annual Burned Area[a]

Region	Start Month	Mean Annual Area Burned (Mha)	CV[b]	Full Series Trend Absolute (Mha yr^{-1})	Full Series Trend Relative (% yr^{-1})	MODIS-Era Trend Absolute (Mha yr^{-1})	MODIS-Era Trend Relative (% yr^{-1})
Global	May	349.7	0.07	−3.6	−1.0	−4.3	−1.2
BONA	April	2.2	0.59	+0.07	+3.1	+0.05	+2.2
TENA	Jan.	1.8	0.39	+0.002	+0.1	+0.02	+0.8
CEAM	Oct.	1.8	0.46	−0.04	−2.4	+0.02	+1.4
NHSA	July	2.6	0.36	−0.03	−1.5	−0.1	−5.6
SHSA	May	18.7	0.43	−0.6	−3.2	−0.3	−1.9
EURO	Feb.	0.7	0.37	−0.04	−5.3	−0.06	−9.5
MIDE	May	0.8	0.35	+0.03	+3.9	+0.07	+9.5
NHAF	Aug.	117.7	0.07	−1.3	−1.1	−1.7	−1.4
SHAF	March	125.0	0.08	+1.5	+1.2	+2.3	+1.8
BOAS	Feb.	5.6	0.69	+0.01	+0.2	−0.2	−2.7
CEAS	Jan.	13.6	0.33	+0.2	+1.7	−0.02	−0.1
SEAS	Sep.	7.0	0.28	+0.2	+2.5	+0.2	+2.8
EQAS	Jan.	1.6	1.07	−0.04	−2.5	−0.02	−1.5
AUST	April	50.2	0.46	−2.8	−5.6	−5.5	−10.7

[a]Computed on the basis of region-specific fire years commencing in the specified calendar month ("Start Month"). Trends (the slopes of the robust regression lines) are shown for both the full GFED4 time series and the MODIS-era subset (August 2000 onward). Also shown are the mean annual burned area and coefficient of variation (CV) of annual area burned for each region. The precise time period represented by the mean and CV varies slightly by region since the July 1996 start date of the continuous GFED4 data record does not coincide with the beginning of the fire year for any region except NHSA.
[b]The coefficient of variation is defined as the standard deviation of a random variable X divided by the mean of X.

by calendar year.) To help identify trends, we fitted robust regression lines using the approach recommended by *Tukey* [1977] to reduce the impact of anomalous fire years that would significantly bias ordinary least squares regression (e.g., the 1997–1998 ENSO event seen in EQAS). Due to the larger uncertainties accompanying the pre-MODIS burned area estimates, we fitted separate trend lines to the full time series as well as the shorter MODIS-era subset (Table 1) and use greater caution in basing conclusions upon the former.

[24] At 16 years, the GFED4 time series remains too short to reliably identify long-term trends; thus, as with previous versions of the data set, we will consider only the most pronounced: (1) a gradual decrease of 1.7 Mha yr^{-1} (−1.4% yr^{-1}) in NH Africa since 2000; (2) a gradual increase of 2.3 Mha yr^{-1} (+1.8% yr^{-1}) in SH Africa also since 2000; (3) a slight increase of 0.2 Mha yr^{-1} (+2.5% yr^{-1}) in Southeast Asia since 1997; and (4) a rapid although inconsistent decrease of approximately 5.5 Mha yr^{-1} (−10.7% yr^{-1}) from 2001 through 2010 in Australia, followed by a major upsurge in 2011 that exceeded the annual area burned in at least the previous 14 years. The net trend in global burned area from 2000 to 2012 was a modest decrease of 4.3 Mha yr^{-1} (−1.2% yr^{-1}). The conflicting burned area trends in Africa may be related to the increase in net primary productivity (NPP) observed in NH Africa from 2000 to 2009 and the drought-related decline in NPP observed in SH Africa during the same time period [*Zhao and Running*, 2010].

5.2. Interannual Variability

[25] We quantified interannual variability with the coefficient of variation (CV) for the annual area burned within each region (Figure 8 and Table 1). On the basis of this metric, we identify four main groups. The first group, which is characterized by low coefficients of variation (≈0.075), is composed of SH and NH Africa, where the area burned
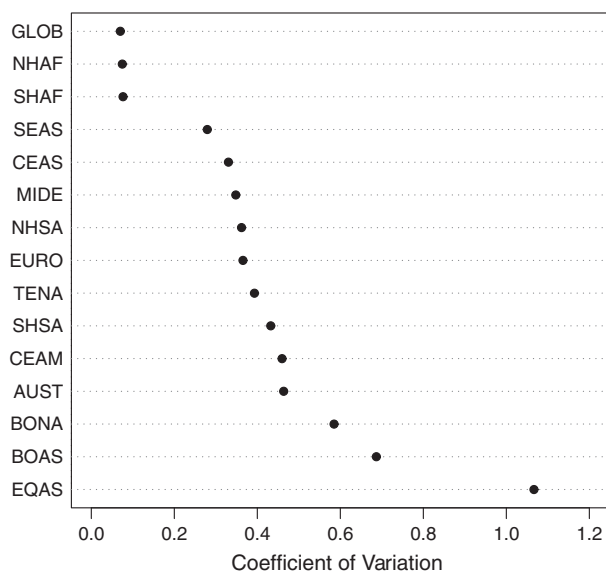

Figure 8. Interannual variability of burned area for each region, expressed in terms of the coefficient of variation of annual burned area from July 1996 through August 2012. Annual burned area totals were computed with respect to the region-specific fire years as defined in Figure 6.

is exceedingly large and highly regular each fire season. Because the global time series is overwhelmingly dominated by Africa, the global case falls in this group as well. The second group contains nine regions [SEAS, CEAS, MIDE, NHSA, Europe (EURO), Temperate North America (TENA), SHSA, Central America (CEAM), and AUST], within which the CV varies from 0.28 to 0.46. Comprising the third group are the two boreal regions, Boreal
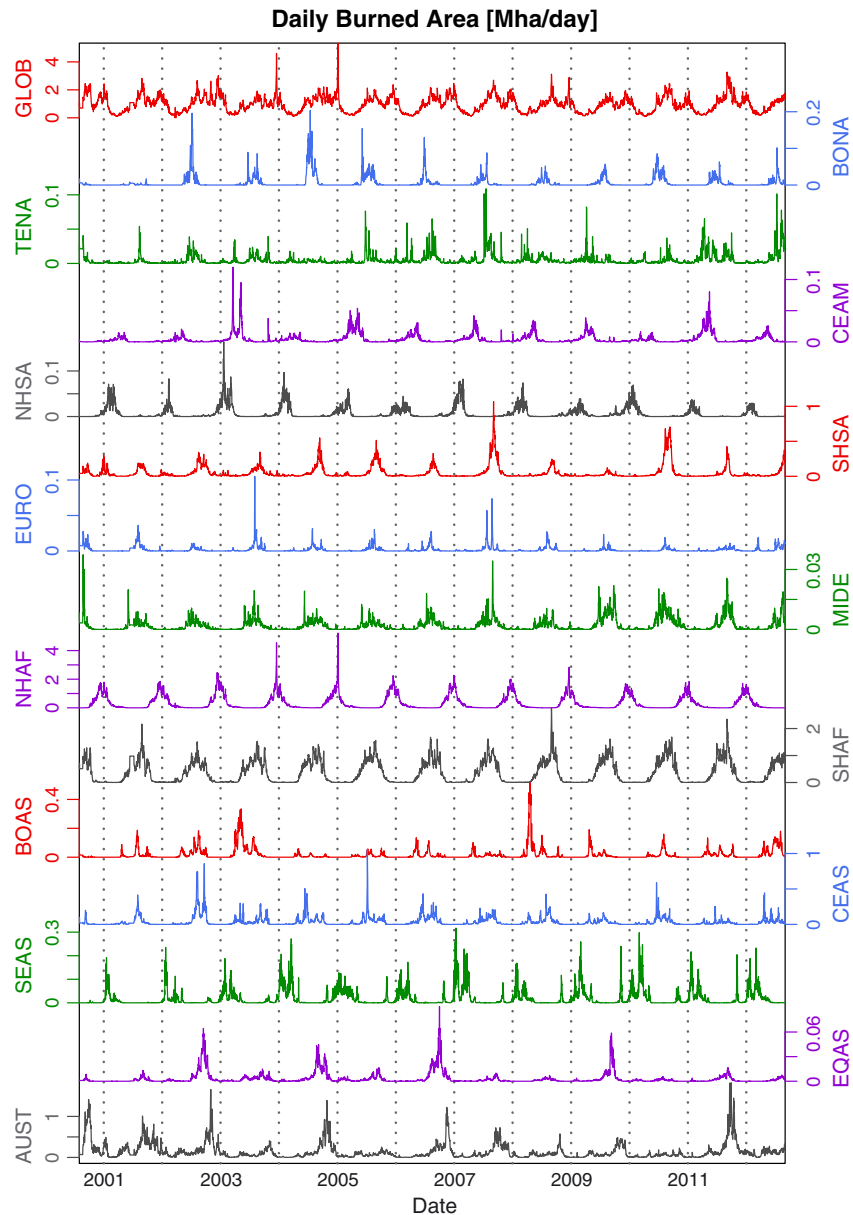
Figure 9. Worldwide and regional 1 August 2000 to 31 August 2012 GFED4 daily burned area time series.

North America (BONA) and Boreal Asia (BOAS), which exhibit somewhat higher interannual variability (CV = 0.59 and 0.69, respectively) due to the more episodic nature of large fires in these regions. The last group consists of a single region (Equatorial Asia) and is characterized by very high interannual variability (CV= 1.07). This is primarily because fire activity within Equatorial Asia is strongly associated with ENSO events [*Fuller and Murphy*, 2006; *Giglio et al.*, 2010], with significantly more area burned during the warmer, dry El Niño phases (e.g., 1998, 2002, 2004, 2006, and 2009) and correspondingly less area burned during the cooler, wet La Niña phases (e.g., 1999, 2000, 2008, 2010). The progression of increasing CV depicted in Figure 8 reflects a general transition from widespread and routine human-induced burning (primarily for land maintenance), coupled with lower interannual rainfall variability,

to more sporadic ignition of fires (by humans or otherwise) in combination with greater rainfall variability.

6. Analysis of Daily Time Series

[26] The GFED4 regional daily burned area time series are shown in Figure 9. As expected, in all regions there is considerably more temporal variability than portrayed in the monthly time series. Among other benefits, this finer time step has the potential to improve fire emissions estimates by allowing emission factors and/or combustion completeness to be more realistically adjusted using daily precipitation and other observations that influence fuel moisture levels. Particularly regular and distinct burning seasons are apparent in both SH and NH Africa, where the time series reveal distinct seasonal peaks reaching
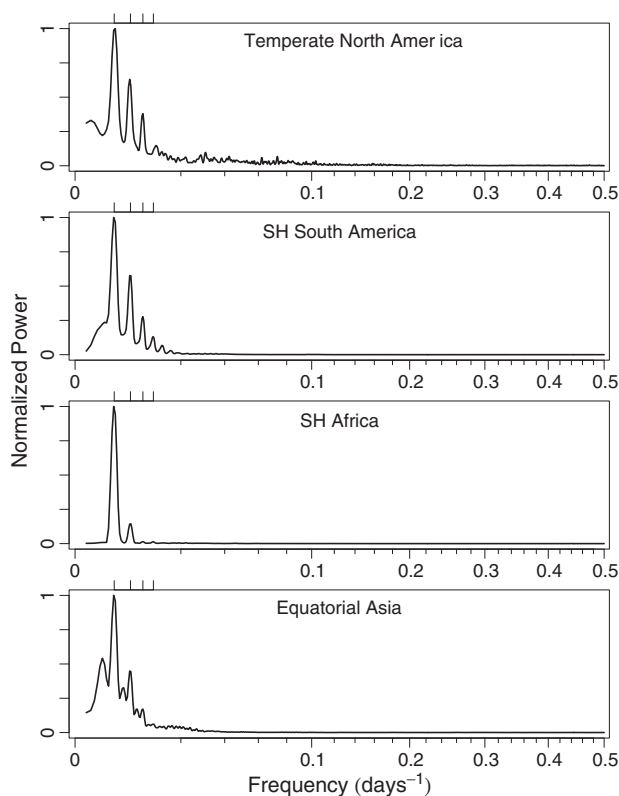
Figure 11. Mean uncertainty in burn date for the 1 August 2000 to 31 August 2012 GFED4 daily burned area time series. See Table S4 in Text S1 of the supporting information for a regional summary of this uncertainty.

we found a significant 2 year cycle for Equatorial Asia, a byproduct of the sequence of ENSO events (often at 2 year intervals, including 2002, 2004, 2006, and 2009) occurring throughout the GFED4 daily time series.

7. Caveats and Limitations

[28] As with any remotely sensed data set, there are important caveats and limitations that should be considered when using the GFED4 burned area data set. First, despite adjustments made to the DB mapping algorithm (section 2.1), the underlying MCD64A1 burned area maps have a minimum detectable burn size of ~40 ha in cropland, which still exceeds the size of many agricultural waste burns [*McCarty et al.*, 2007]. To some unknown degree, GFED4 therefore underestimates the extent of cropland burning. Using active fire observations to statistically restore these and other small burns might be possible, provided that adequate calibration data are available, and is an active area of research [e.g., *McCarty et al.*, 2009; *Randerson et al.*, 2012]. Second, cloud cover degrades the detection of both active fires and fire scars; thus, burned area in persistently cloudy regions may be systematically underestimated. An important next step is to quantify the extent of this potential bias, possibly with ground-based or airborne observations since conventional validation using high-resolution, optical satellite imagery is itself confounded by cloud cover. Finally, the spatial and temporal variation in cloud persistence in turn introduces spatial and temporal variability in the likelihood of omission errors, the uncertainties in the monthly and daily burned area estimates, and the temporal uncertainty in the daily burned area time series. As an example, the mean uncertainty in the burn date recorded in the daily time series is shown in Figure 11 and reveals that, in addition to having high spatial variability, the temporal uncertainty in persistently cloudy regions can be many times larger than the underlying temporal resolution of the data set itself.

8. Conclusions

[29] We have described the fourth generation of the Global Fire Emissions Database (GFED4) burned area data set, which provides global monthly burned area at 0.25° spatial resolution from mid-1995 through the present and higher-resolution daily burned area for a subset of the time series extending back to August 2000. During the MODIS era (August 2000 onward), the data set was derived

Figure 10. Normalized periodograms of the 1 August 2000 to 31 August 2012 GFED4 daily burned area time series for four representative regions. The four tick marks at the top of each plot indicate, from left to right, the fundamental frequency (f = 0.00274 days^{-1}) corresponding to a period (T) of 1 year, followed by the locations of harmonics at $2f$ (T = 6 months), $3f$ (T = 4 months), and $4f$ (T = 3 months).

~2 Mha day^{-1}. In both 2003 and 2004, the maximum daily area burned in NHAF exceeded 4 Mha day^{-1}, which is equivalent to burning an average of one half million square meters of vegetation each second over a 24 h period. The majority of the area burned during these peak periods was consistently located within the same contiguous patch spanning southern Chad, the Central African Republic, and South Sudan noted in section 4.1. While our earlier trend analysis revealed only a slight upward trend in the annual area burned for Temperate North America since 2000, the daily time series suggests that the number of days during which significant burning occurs each year is increasing as well.

[27] We also computed the Lomb periodogram for each time series. Representative results are shown in Figure 10. The power spectrum in all regions showed a dominant annual cycle accompanied by numerous higher-frequency harmonics characteristic of time series resembling a train of distinct pulses. No vestiges of the 16 day MODIS repeat cycle (frequency ≈ 0.06 day^{-1}) were observed for any region, a result that was expected since the MCD64A1 burned-area mapping algorithm uses 10 day moving averages to remove BRDF effects from the daily input data required for processing. With respect to lower frequencies,
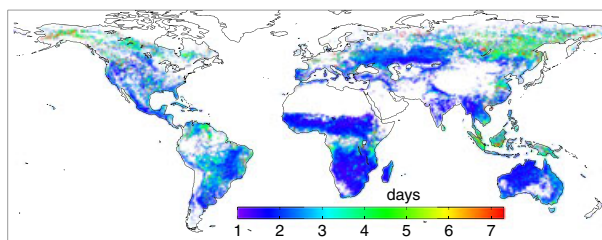
[30] In terms of area burned, savanna fires were overwhelmingly dominant in both SH and NH Africa (90% and 82% of the total area burned, respectively) and somewhat less so in SH South America (65%). Forest fires (either wildfires or those burning in the deforestation process) comprised the largest proportion of area burned in Equatorial Asia (62%), followed by Boreal North America (48%) and Boreal Asia (36%). Grassland fires were the most prevalent in Central Asia and NH South America, while cropland fires were dominant in Europe and the Middle East. Shrubland burning comprised a relatively small proportion of the area burned in all regions except Australia, where 37% of the area burned belonged to this category.

[31] We assessed the interannual variability and trends in burned area on the basis of a region-specific definition of fire years. With respect to trends, we found a gradual decrease of 1.7 Mha yr^{-1} (–1.4% yr^{-1}) in NH Africa since 2000, a gradual increase of 2.3 Mha yr^{-1} (+1.8% yr^{-1}) in SH Africa also since 2000, a slight increase of 0.2 Mha yr^{-1} (+2.5% yr^{-1}) in Southeast Asia since 1997, and a rapid decrease of approximately 5.5 Mha yr^{-1} (–10.7% yr^{-1}) from 2001 through 2011 in Australia, followed by a major upsurge in 2011 that exceeded the annual area burned in at least the previous 14 years. The net trend in global burned area from 2000 to 2012 was a modest decrease of 4.3 Mha yr^{-1} (–1.2% yr^{-1}).

[32] We performed a spectral analysis of the daily burned area time series and found no vestiges of the 16 day MODIS repeat cycle in any region, a result that was expected since the MCD64A1 burned-area mapping algorithm uses 10 day moving averages to remove BRDF effects from the daily input data required for processing. In addition to the expected annual cycle and higher-frequency harmonics present in all regions, we found a significant 2 year cycle in Equatorial Asia, a byproduct of the sequence of ENSO events (often at 2 year intervals) occurring throughout the time period covered by GFED4. In addition to depicting considerably more temporal variability than portrayed in the monthly time series, the daily burned area time series affords the possibility of adjusting emission factors and/or combustion completeness in emissions models based on daily precipitation records, thus helping to improve emissions estimates.

[33] There is considerable value in continuing and maintaining long-term, global burned area data sets such as GFED. In the short term, this objective can be met with burned area maps derived from MODIS imagery since both the Terra and Aqua satellites have sufficient fuel reserves to remain functional for at least another 5 years. Beyond this time frame, the most practical replacements for MODIS are the Visible Infrared Imaging Radiometer Suite (VIIRS), on-board the Suomi-NPP (National Polar-orbiting Partnership) satellite and the forthcoming series of Joint Polar Satellite System (JPSS) spacecraft [*Murphy et al.*, 2006], and the Sea and Land Surface Temperature Radiometer (SLSTR) on-board ESA's forthcoming Sentinel-3 satellite pair [*Coppo et al.*, 2010]. Extending GFED further into the past is equally desirable, although any such endeavor is extremely challenging due to the availability of neither global active fire data suitable for calibration nor spectrally suitable reflectance imagery from which burned areas can be mapped. To date, most efforts to develop pre-MODIS historical records of burned area have relied on coarse resolution Global Area Coverage (GAC) observations from the Advanced Very High Resolution Radiometer (AVHRR) series of sensors [e.g., *Barbosa et al.*, 1999; *Carmona-Moreno et al.*, 2005]. However, none yet fully compensate for temporal artifacts caused by instrument switching, sensor saturation, and the pervasive orbital drift of the NOAA Polar Orbiting Environmental Satellites (POES) [*Csiszar et al.*, 2003; *Giglio*, 2007]. The GFED4 gridded 0.25° monthly and daily burned area data sets are available through the web site http://www.globalfiredata.org and will be updated regularly.

References

Arino, O., and J.-M. Rosaz (1999), 1997 and 1998 world ATSR fire atlas using ERS-2 ATSR-2 data, in *Proceedings of the Joint Fire Science Conference and Workshop*, edited by L. F. Neuenschwander, K. C. Ryan, and G. E. Gollberg, vol. 1, University of Idaho and the International Association of Wildland Fire, Boise, Idaho, 177–182.

Barbosa, P. M., J.-M. Grégoire, and J. M. C. Pereira (1999), An algorithm for extracting burned areas from time series of AVHRR GAC data applied at a continental scale, *Remote Sensing of Environment*, 69, 253–263.

Boschetti, L., and D. P. Roy (2008), Defining a fire year for reporting and analysis of global interannual fire variability, *Journal of Geophysical Research*, 113, G03020, doi:10.1029/2008JG000686.

Carmona-Moreno, C., A. Belward, J.-P. Malingreau, A. Hartley, M. Garcia-Alegre, M. Antonovskiy, V. Buchshtaber, and V. Pivovarov (2005), Characterizing interannual variations in global fire calendar using data from Earth observing satellites, *Global Change Biol.*, 11, 1537–1555, doi:10.1111/j.1365-2486.2005.001003x.

Coppo, P. et al. (2010), SLSTR: A high accuracy dual scan temperature radiometer for sea and land surface monitoring from space, *J. Mod. Optic.*, 57(18), 1815–1830, doi:10.1080/500340.2010.503010.

Csiszar, I., A. Abuelgasim, Z. Li, J.-Z. Jin, R. Fraser, and W.-M. Hao (2003), Interannual changes of active fire detectability in North America from long-term records of the advanced very high resolution radiometer, *J. Geophys. Res.*, 108(D2), 4075–4084, doi:10.1029/2001JD001373.

Friedl, M. A., D. Sulla-Menashe, B. Tan, A. Schneider, N. Ramankutty, A. Sibley, and X. Huang (2010), MODIS Collection 5 global land cover: Algorithm refinements and characterization of new datasets, *Rem. Sens. Environ.*, 114, 168–182, doi:10.1016/j.rse.2009.08.016.

Fuller, D. O., and K. Murphy (2006), The ENSO-fire dynamic in insular southeast Asia, *Climatic Change*, 74, 435–455, doi:10.1007/s10584-006-0432-5.

Giglio, L. (2007), Characterization of the tropical diurnal fire cycle using VIRS and MODIS observations, *Rem. Sens. Environ.*, 108, 407–421, doi:10.1016/j.rse.2006.11.018.

Giglio, L., J. D. Kendall, and R. Mack (2003a), A multi-year active fire data set for the tropics derived from the TRMM VIRS, *Int. J. Rem. Sens.*, 24(22), 4505–4525, doi:10.1080/0143116031000070283.

Giglio, L., J. Pinzon, and P. S. Kasibhatla (2003b), Comment on "Seasonal, intraseasonal, and interannual variability of global land fires and their effects on atmospheric aerosol distribution" by Y. Ji and E. Stocker, *J. Geophys. Res.*, 108(D24), 4754, doi:10.1029/2003JD003548.

Giglio, L., G. R. van der Werf, J. T. Randerson, G. J. Collatz, and P. S. Kasibhatla (2006), Global estimation of burned area using MODIS active fire observations, *Atmos. Chem. Phys.*, 6, 957–974, doi:10.5194/acp-6-957-2006.

Giglio, L., T. Loboda, D. P. Roy, B. Quayle, and C. O. Justice (2009), An active-fire based burned area mapping algorithm for the MODIS sensor, *Rem. Sens. Environ.*, *113*, 408–420, doi:10.1016/j.rse.2008.10.006.

Giglio, L., J. T. Randerson, G. R. van der Werf, P. S. Kasibhatla, G. J. Collatz, D. C. Morton, and R. S. Defries (2010), Assessing variability and long-term trends in burned area by merging multiple satellite fire products, *Biogeosciences*, *7*, 1171–1186, doi:10.5194/bg-7-1171-2010.

Hoelzemann, J., M. Schultz, G. Brasseur, C. Granier, and M. Simon (D14S04), Global Wildland Fire Emission model (GWEM): Evaluating the use of global area burnt satellite data, *J. Geophys. Res.*, *109*, doi: 10.1029/2003JD003666.

Lamarque, J.-F. et al. (2010), Historical (1850–2000) gridded anthropogenic and biomass burning emissions of reactive gases and aerosols: Methodology and application, *Atmos. Chem. Phys.*, *10*(15), 7017–7039, doi:10.5194/acp-10-7017-2010.

Liousse, C. et al. (2010), Updated African biomass burning emission inventories in the framework of the AMMA-IDAF program, with an evaluation of combustion aerosols, *Atmos. Chem. Phys.*, *10*(19), 9631–9646, doi:10.5194/acp-10-9631-2010.

Loboda, T. V., E. E. Hoy, L. Giglio, and E. S. Kasischke (2011), Mapping burned area in Alaska using MODIS data: A data limitations-driven modification to the regional burned area algorithm, *Int. J. Wildland Fire*, *20*, 487–496, doi:10.1071/WF10017.

Loboda, T. V., L. Giglio, L. Boschetti, and C. O. Justice (2012), Regional fire monitoring and characterization using global NASA MODIS fire products in dry lands of Central Asia, *Front. Earth. Sci.*, *6*(2), 196–205, doi:10.1007/s11707-012-0313-3.

McCarty, J., C. O. Justice, and S. Korontzi (2007), Agricultural burning in the southeastern United States detected by MODIS, *Rem. Sens. Environ.*, *108*, 151–162, doi:10.1016/j.rse.2006.03.020.

McCarty, J. L., S. Korontzi, C. O. Justice, and T. Loboda (2009), The spatial and temporal distribution of crop residue burning in the contiguous United States, *Sci. Total Environ.*, *407*(21), 5701–5712, doi:10.1016/j.scitotenv.2009.07.009.

Murphy, R. E., P. Ardanuy, F. J. Deluccia, J. E. Clement, and C. F. Schueler (2006), The visible infrared imaging radiometer suite, in *Earth Science Remote Sensing: Science and Instruments*, edited by J.J. Qu, W. Gao, M. Kafatos, R.E. Murphy, and V.V. Salomonson, Tsinghua University Press and Springer-Verlag, Beijing, 199–223.

Pereira, J. M. C., M. J. P. Vasconcelos, and A. M. Sousa (2000), A rule-based system for burned area mapping in temperate and tropical regions using NOAA/AVHRR imagery, in *Biomass Burning and its Inter-Relationships with the Climate System*, edited by J.L. Innes, M. Beniston, and M.M. Verstraete, Kluwer Academic Publishers, Dordrecht, 215–232.

Randerson, J. T., Y. Chen, G. R. van der Werf, B. M. Rogers, and D. C. Morton (2012), *Journal of Geophysical Research*, *117*, G04,012, doi:10.1029/2012JG002128.

Schultz, M. G., A. Heil, J. J. Hoelzemann, A. Spessa, K. Thonicke, J. Goldammer, A. C. Held, and J. M. Pereira (2008), Global emissions from wildland fires from 1960 to 2000, *Global Biogeochem. Cy.*, *22*, GB2002, doi:10.1029/2007GB003031.

Townshend, J. R. G., M. Carroll, C. Dimiceli, R. Sohlberg, M. Hansen, and R. S. DeFries (2011), *MODIS Collection 5 Vegetation Continuous Fields (MOD44B) Percent Tree Cover, Digital data accessed 28 Dec. 2011 from http://reverb.echo.nasa.gov/reverb/*.

Tsela, P. L., P. van Helden, P. Frost, K. Wessels, and S. Archibald (2010), Validation of the MODIS burned-area products across different biomes in South Africa, in *Proceedings of the International Geoscience and Remote Sensing Symposium*, IEEE Computer Society, Honolulu, Hawaii, 3652–3655, doi:10.1109/IGARSS.2010.5650253, (to appear in print).

Tukey, J. W. (1977), *Exploratory Data Analysis*, Addison-Wesley, Reading.

Urbanski, S. P., W. M. Hao, and B. Nordgren (2011), The wildland fire emission inventory: Western United States emission estimates and an evaluation of uncertainty, *Atmos. Chem. Phys.*, *11*, 12,973–13,000, doi: 10.5194/acp-11-12973-2011.

van der Werf, G. R., J. T. Randerson, L. Giglio, G. J. Collatz, P. S. Kasibhatla, and A. F. Arellano Jr. (2006), Interannual variability of global biomass burning emissions from 1997 to 2004, *Atmos. Chem. Phys.*, *6*, 3423–3441, doi:10.5194/acp-6-3423-2006.

van der Werf, G. R., J. T. Randerson, L. Giglio, G. J. Collatz, M. Mu, P. S. Kasibhatla, D. C. Morton, R. S. DeFries, Y. Jin, and T. T. van Leeuwen (2010), Global fire emissions and the contribution of deforestation, savanna, forest, agricultural, and peat fires (1997–2009), *Atmos. Chem. Phys.*, *10*, 11,707–11,735, doi:10.5194/acp-10-11707-2010.

Wolfe, R. E., D. P. Roy, and E. Vermote (1998), MODIS land data storage, gridding, and compositing methodology: Level 2 grid, *IEEE Trans. Geosci. Rem. Sens.*, *36*, 1324–1338.

Zhao, M., and S. W. Running (2010), Drought-induced reduction in global terrestrial net primary production from 2000 through 2009, *Science*, *329*, 940–943, doi:10.1126/science.1192666.